Langmuir Circulations Transfer Kinetic Energy from Submesoscales and Larger Scales to Dissipative Scales

DELPHINE HYPOLITE,[a] LEONEL ROMERO,[b] JAMES C. MCWILLIAMS,[a] AND DANIEL P. DAUHAJRE[a]

[a] *Department of Atmospheric and Oceanic Sciences, University of California, Los Angeles, Los Angeles, California*
[b] *Department of Marine Sciences, University of Connecticut, Groton, Connecticut*

(Manuscript received 10 June 2022, in final form 23 September 2022)

ABSTRACT: Surface gravity wave effects on currents (WEC) cause the emergence of Langmuir cells (LCs) in a suite of high horizontal resolution ($\Delta x = 30$ m), realistic oceanic simulations in the open ocean of central California. During large wave events, LCs develop widely but inhomogeneously, with larger vertical velocities in a deeper mixed layer. They interact with extant submesoscale currents. A 550-m horizontal spatial filter separates the signals of LCs and of submesoscale and larger-scale currents. The LCs have a strong velocity variance with small density gradient variance, while submesoscale currents are large in both. Using coarse graining, we show that WEC induces a forward cascade of kinetic energy in the upper ocean up to at least a 5-km scale. This is due to strong positive vertical Reynolds stress (in both the Eulerian and the Stokes drift energy production terms) at all resolved scales in the WEC solutions, associated with large vertical velocities. The spatial filter elucidates the role of LCs in generating the shear production on the vertical scale of Stokes drift (10 m), while submesoscale currents affect both the horizontal and vertical energy fluxes throughout the mixed layer (50–80 m). There is a slightly weaker forward cascade associated with nonhydrostatic LCs (by 13% in average) than in the hydrostatic case, but overall the simulation differences are small. A vertical mixing scheme *K*-profile parameterization (KPP) partially augmented by Langmuir turbulence yields wider LCs, which can lead to lower surface velocity gradients compared to solutions using the standard KPP scheme.

KEYWORDS: Energy transport; Small scale processes; Oceanic waves; Nonhydrostatic models

1. Introduction

Langmuir circulations (Langmuir 1938) or Langmuir cells (LCs) can be identified by concentrated horizontal convergence and downwelling lines in the upper ocean. They are generated under strong winds and waves conditions that are typical in the ocean (Belcher et al. 2012). The cells have a narrow width $\mathcal{O}(10–100)$ m. They may extend longitudinally up to $\mathcal{O}(1)$ km, or even longer in strong swell (McWilliams et al. 2014). They are generally aligned with the wind direction even though they are sensitive to wave and current directions as well (Van Roekel et al. 2012; Shrestha et al. 2019). An early theoretical interpretation of LCs is from the Craik and Leibovich (1976) equations where they originate from a wave–current instability in which the Stokes drift vertical shear tilts vertical vorticity anomalies into the horizontal through the action of the Stokes vortex (or shear) force (Craik 1977; Thorpe 2004; Suzuki et al. 2016). A multiscale asymptotic theory for the phase-averaged dynamics of low-frequency motions in the presence of high-frequency surface gravity waves with Stokes drift (McWilliams et al. 2004) provides a widely used theoretical framework for LCs in large-eddy simulation (LES) models (McWilliams et al. 1997; Harcourt and D'Asaro 2008)—see the review of Sullivan and McWilliams (2010)—and more recently this practice has been extended to circulation models (Uchiyama et al. 2010).

Surface gravity waves and submesoscale currents (SMCs) interact in the upper ocean, along with small-scale (boundary layer) turbulent motions, including Langmuir turbulence. McWilliams and Fox-Kemper (2013) find that wave effects are potentially important in the mesoscale and submesoscale regime [also see Suzuki and Fox-Kemper (2016)]. Submesoscale currents take the form of fronts, filaments, and vortices on scales $\mathcal{O}(0.1–1)$ km and are identified by large ageostrophic vertical velocities, buoyancy gradients, surface convergence, and cyclonic relative vorticity. More generally submesoscale currents are characterized by large Rossby number $\mathrm{Ro} = V/fl > 1$, where V is a horizontal velocity scale, l a horizontal length scale, and f the Coriolis frequency (Thomas et al. 2008; Romero et al. 2013; McWilliams 2016; Dauhajre et al. 2017; Wu et al. 2021). They constitute an efficient way to transfer energy from mesoscales to dissipative scales (Klein and Lapeyre 2009; Gula et al. 2014), and a recent study demonstrates that this forward cascade of kinetic energy is driven by frontogenesis at submesoscale fronts (Srinivasan et al. 2022). The challenge to understanding the coupling between surface gravity waves and currents resides in the fact that there are interactions across scales; that is, large temporal and spatial scales can be sensitive to small-scale processes, particularly in the oceanic and atmospheric turbulent boundary layers.

LES modeling is beginning to be used for SMC studies, such as that of Skyllingstad and Samelson (2012), which shows enhanced turbulence associated with baroclinic waves. Suzuki et al. (2016) and McWilliams (2018) show how surface gravity waves can modify specific submesoscale phenomena. Fronts are stronger when the main frontal axis is aligned with the Stokes shear. Hamlington et al. (2014) show that Langmuir turbulence counters the restratifying effects of submesoscale eddies leading to enhanced small-scale vertical transport and mixing. At submesoscale fronts, the vortex force modifies the

Corresponding author: Delphine Hypolite, dhypolite@atmos.ucla.edu

DOI: 10.1175/JPO-D-22-0126.1

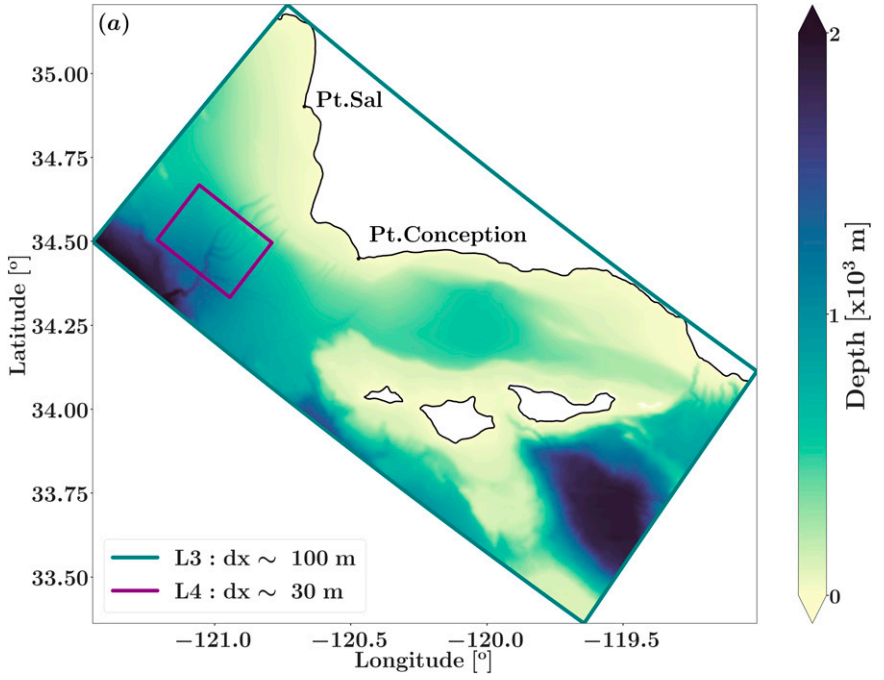

FIG. 1. The Regional Oceanic Modeling System (ROMS) domains defined in central California at two horizontal resolutions: the L3 domain delimited in teal with an average horizontal spacing $dx = 100$ m and the L4 domain in purple with $dx = 30$ m with colors showing bathymetry.

thermal wind balance (Li et al. 2012; Haney et al. 2015; Sullivan and McWilliams 2019), which ultimately impacts ocean tracers (Smith et al. 2016).

In a previous study based on Regional Oceanic Modeling System (ROMS) simulations in realistic oceanic settings including surface wave effects, at $\Delta x \simeq 270$ and 100 m horizontal resolution, and using the vertical mixing scheme K-profile parameterization (KPP; Large et al. 1994), Hypolite et al. (2021, hereafter HRMD21) show that surface gravity wave effects on submesoscale dynamics are important when waves are of relatively large amplitude (when the average wave amplitude is $A_{\text{wave}} = H_s/2\sqrt{2} > 1.5$ m with H_s the significant wave height). In the Langmuir turbulence regime (i.e., when the turbulent Langmuir number $\text{La}_t = \sqrt{U^*/U^{\text{St}}}$ is lower than about 0.5, where U^* is the friction velocity and U^{St} the surface Stokes drift magnitude), roll-cells appear near the surface in hydrostatic configurations but with widths that are larger than familiar LCs from measurements and LES. This width discrepancy was likely influenced by to the model grid resolution.

The present article builds on HRMD21 and investigates the coupling between Langmuir turbulence and submesoscale dynamics at higher horizontal resolution $\Delta x \simeq 30$ m with ROMS. Here, we assess both the resolution influence and nonhydrostatic consequences (Roullet et al. 2017) of surface waves on the submesoscale dynamics and development of Langmuir roll-cells. We also examine the impacts of the vertical mixing scheme KPP when partially enhanced by Langmuir turbulence following the prescription of Li and Fox-Kemper (2017). We describe the model configuration in section 2. We show how a uniform spatial filter at 550 m can separate the signal of the resolved LCs from the larger-scale flow (including the SMCs) and provide a dynamical description of the LCs in a submesoscale regime. In section 3, we appraise the cross-scale flux of kinetic energy by employing the filter-based coarse graining framework across spatial scales (Aluie et al. 2018; Schubert et al. 2020). This provides evidence that the LCs are engendering a forward cascade of energy from SMCs to dissipative small scales. This study demonstrates that LCs can emerge inhomogenously at times of smooth (nearly homogeneous) wind and wave forcing in section 4. Section 5 summarizes the findings and discusses the caveats and limitations of our approach along with the need for higher-resolution realistic and idealized simulations.

2. Modeling

a. *ROMS configuration*

We conduct numerical simulations in central California using ROMS (Shchepetkin and McWilliams 2005) with gradual nesting to zoom on an open ocean region offshore from Point Conception (see the purple domain labeled L4 in Fig. 1) for a period in December 2006. This region has rich mesoscale and submesoscale eddy fields as part of the California Current System (Capet et al. 2008) and in winter is well exposed to North Pacific storms and westerly wind generated waves. The nearby Channel Islands (located southeast outside of the L4 domain) constitute an important source for mesoscale (and submesoscale) eddies. These topographically generated eddies are advected by the regional circulation north and

TABLE 1. Configuration of ROMS runs for the central California L4 open ocean region.

Simulation	NO WEC	WEC	WEC NH	WEC KPP+	WEC NH KPP+
WEC		✓	✓	✓	✓
Nonhydrostatic			✓		✓
Vertical mixing scheme	KPP	KPP	KPP	KPP+	KPP+
Time period	Events 1–2	Events 1–2	Event 1	Events 1–2	Events 1–2
Boundary conditions	L3 WEC KPP	L3 WEC KPP	L3 WEC KPP	L3 WEC KPP+	L3 WEC KPP+

westward, penetrating at times the L4 domain, with meanders evolving into submesoscale structures. The L4 horizontal grid size 1026×770 allows small grid spacing $\Delta x = 30$ m in an active submesoscale regime interacting with surface gravity waves with 128 vertical levels and with the stretching parameters $h_{\text{cline}} = 25$ m, $\theta_b = 6$, and $\theta_c = 6$. This gives a grid-scale aspect ratio $\Delta x/\Delta z \sim N/f$ near the surface, where N is the stratification, well suited for simulating small-scale processes (Ménesguen et al. 2018). We use a 100-m horizontal resolution run (L3 teal domain in Fig. 1) presented in HRMD21 as parent to force hourly the L4 domain at the boundaries during two large wave amplitude events ($A_{\text{wave}} = H_s/2\sqrt{2} > 1.5$ m, with H_s being the significant wave height) in December 2006. Event 1 is a remote west swell event during 9–14 December 2006 (5 days); event 2 involves westerly wind generated waves during 27–28 December 2006 (2 days) (Fig. 6, first row). The parent boundary forcings contain the barotropic tide (Egbert and Erofeeva 2002; Egbert et al. 1994). Atmospheric forcings are interpolated from 6-km resolution WRF products (Michalakes et al. 1998; Renault et al. 2016) and force the solution hourly.

ROMS has the capability to account for surface gravity waves affecting currents [abbreviated as wave effects on currents (WEC)] through the implementation of the vortex-force formalism for conservative wave-averaged dynamical effects of waves acting on currents in combination with wave-induced mixing effects (Craik and Leibovich 1976; McWilliams et al. 2004; Uchiyama et al. 2010). These equations are derived following a multiscale asymptotic analysis, where small and fast wave motions are separated from larger, slower motions. For small wave steepness, it filters out the waves and only retains the leading-order wave–current couplings with other scales. Far from shore, we neglect wave dissipation induced by bottom drag and wave breaking (from both topography and steepness here). We leave the question of SMC dynamics with WEC nearshore for future study. For the wave field, we use the approach of Romero et al. (2021) to compute the Stokes drift and related WEC quantities consistently with WW3 simulations that solve the full realistic 2D spectrum of oceanic surface gravity waves.

The present analysis is based on five simulations (Table 1) with the same horizontal grid spacing ($\Delta x = 30$ m). The first solution has no wave forcing (labeled NO WEC). The other four solutions have wave forcings and account for wave–current interactions. The second solution has WEC enabled (labeled WEC), using the hydrostatic approximation. For the third solution, we perform a nonhydrostatic run (Roullet et al. 2017) with WEC (labeled WEC NH). All these solutions use the classic vertical mixing scheme K-profile parameterization (KPP; Large et al. 1994) that gives a vertical profile for eddy viscosity κ_v and tracer diffusivity κ_t. KPP also computes the surface boundary layer depth. It is determined as the minimal depth at which the bulk Richardson number reaches the critical value $\text{Ri}_{\text{cr}} = 0.15$ for high-frequency wind forcing. The local bulk Richardson number takes into account a turbulent velocity scale, product of the Monin–Obukhov scale from the surface buoyancy forcing and the vertical shear of the Eulerian field. We also examine additional effects of waves in an enhanced vertical mixing scheme (labeled KPP+) in another set of nested solutions at both L3 ($\Delta x = 100$ m) and L4 ($\Delta x = 30$ m) with WEC. Note that there are differences in L4 solutions using KPP+ and their KPP counterparts due only to the different boundary conditions that result from modestly divergent evolutions in the parent L3 solutions. KPP+ is implemented in ROMS following elements of Li and Fox-Kemper (2017). It is a minimal modification of KPP that enhances the vertical eddy viscosity by multiplying the turbulent velocity scale by a so-called Langmuir turbulence enhancement factor. This factor depends on the turbulent Langmuir number and relative direction between waves and surface currents. In a stable regime, this factor is

$$\mathcal{E} = 0.8\text{La}_t^{-2/3}\cos\theta_{\text{WC}}, \tag{1}$$

where θ_{WC} is the angle between the wave direction and the surface current. Similarly to the WEC KPP implementation, the eddy viscosity is applied to the Eulerian shear when computing the horizontal momentum fluxes. Equation (1) is a combination of the turbulent variance scaling proposed by Grant and Belcher (2009) and the angular dependency by Van Roekel et al. (2012). Various parameterization schemes for Langmuir turbulence have a large and complicated literature, surveyed by Li and Fox-Kemper (2017), and community consensus has not yet been achieved. For this reason, we view the KPP+ scheme as a provisional sensitivity test of the influence of the choice of a mixing parameterization in the regime reported in this paper with partial resolution of Langmuir roll cells, pending some more complete scheme to be adopted later. Finally, the last solution is produced using nonhydrostatic ROMS, with KPP+ and WEC (labeled KPP+ NH).

For each run, we target the two large-amplitude wave events 1 and 2 (except the WEC NH set, which only covers event 1 because of computational cost) in December 2006, starting two days prior to the beginning of the events to allow the solution to adjust to the grid size downscaling, and we analyze the solution only during the events. We store the instantaneous fields at 15-min output frequency. Nonhydrostatic runs are saved every half hour.

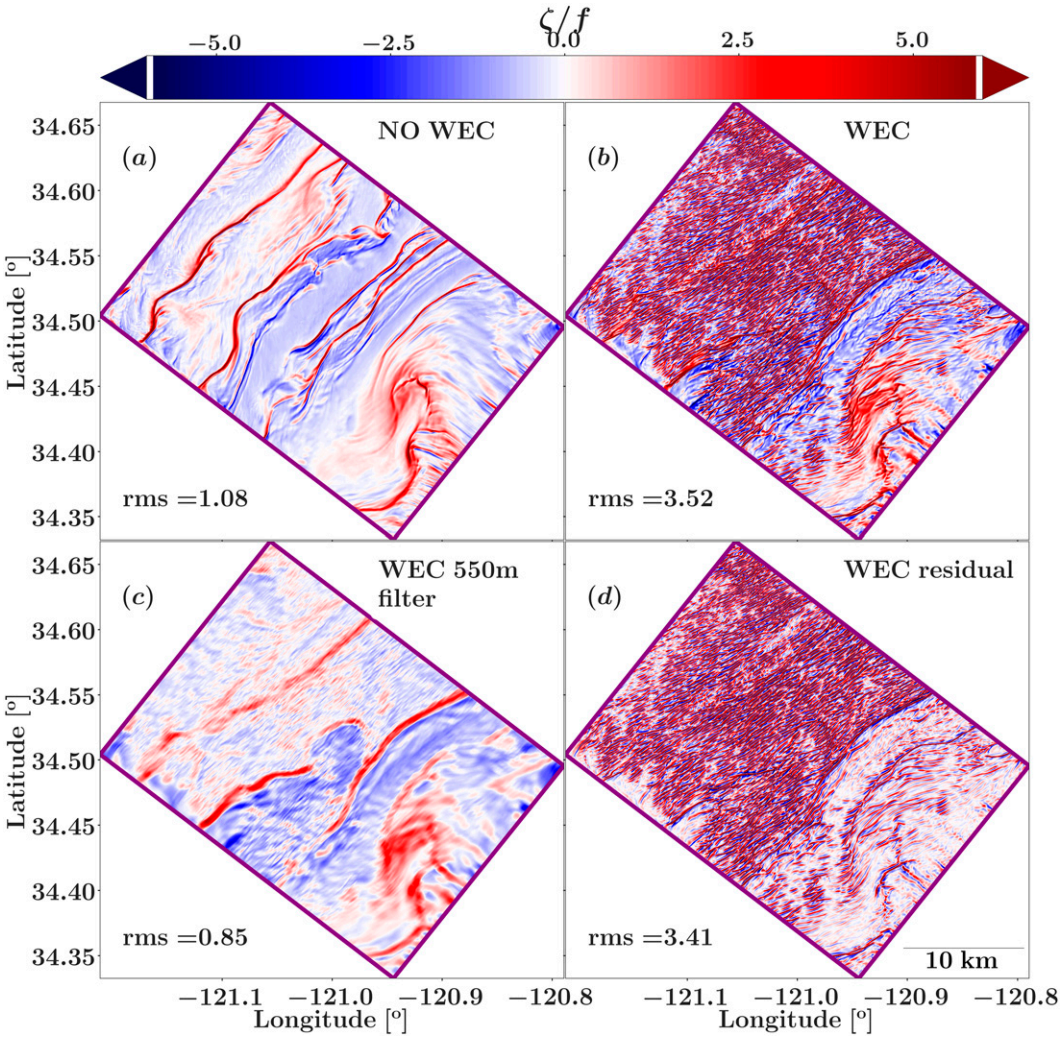

FIG. 2. (a) Snapshot of surface normalized vorticity in the L4 domain at 0400 LT 11 Dec 2006 (event 1) from the solution without wave forcing. (b) As in (a), but from the solution with WEC. (c) A uniform 550-m spatial filter is applied on the solution with WEC. (d) Residual from the solution with WEC and the uniform 550-m spatial filtered solution with WEC. Regions of cyclonic vorticity are in red (anticyclonic regions are in blue). Note that the color bars are saturated. The rms values are shown in insets. For reference, the rms of the filtered solution without wave forcing is 0.71.

b. *Submesoscale flows and Langmuir cell patterns*

During event 1, a remotely generated large wave event, the solutions display detailed SMC structures with a variety of predominantly convergent cyclonic fronts, filaments, and vortices (see Fig. 2a). At times of large waves events like this one, a web of spatially evolving turbulent Langmuir cells (LCs) emerge near surface mostly in solutions that include wave effects on currents; see, for instance, the north part of the domain in Fig. 2b. The solution that does not include the wave effects (NO WEC case) present some roll-cells, but only during event 2 (large local wind-generated waves). These coherent LCs induced by the propagating surface waves (and winds during event 2) have elliptical elongated patterns characterized by alternating signs of large vorticity, divergence, and vertical velocity. The width l_{LC} between the lines here (with $\Delta x = 30$ m) is approximately 160 m in the WEC solution and 200 m in the WEC KPP+ solution. Previous work employing KPP gave $l_{\mathrm{LC}} = 1.8$ and 0.6 km for $\Delta x = 270$ and 100 m respectively (see HRMD21). This suggests that l_{LC} may still scale with resolution, and here it is in the range of the Langmuir scale $\mathcal{O}(10–100)$ m. The LCs are confined to the upper ocean and can extend at times vertically down almost to the entire surface mixed layer depth (between 50 and 80 m on average here) but do not reach as deep as SMCs. Their development is primarily induced by the wave and wind forcing, and once developed they are advected by the ambient flow. We separate the two signals, LCs and SMCs, by applying a uniform $l_f = 550$ m spatial filter (Fig. 2c). The filtered fields contain the SMCs and

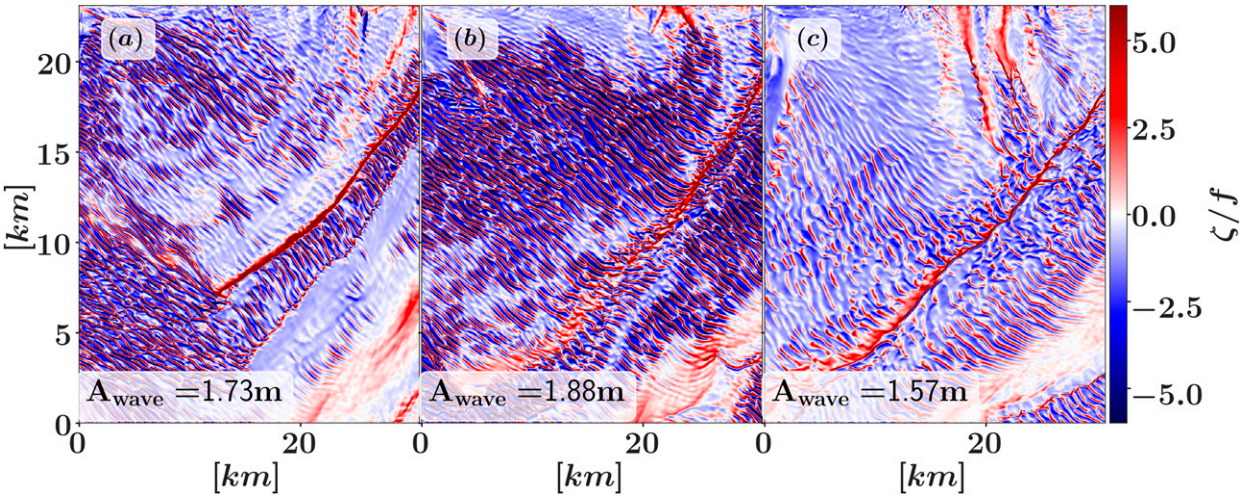

FIG. 3. Sequence of snapshots of surface normalized vorticity in the L4 domain at (a) 0950, (b) 1605, and (c) 2205 LT 14 Dec 2006 (event 1) from the solution with WEC. The average wave amplitude A_{wave} is displayed in each panel. Notice how as A_{wave} increases orthogonal LCs develop and disrupt the large cyclonic trace of a submesoscale front. At these times, the wind is relatively weak and blows upward and to the right; the main wave direction is toward the right; and the mean flow goes downward and to the left.

larger-scale flows (i.e., the mesoscale, wind-driven currents as well as the large-scale regional circulation flow). The residual of this filtering process contains mostly the LCs (Fig. 2e). The vorticity skewness of the low-pass filtered fields is positive and larger than the residual fields. Similarly, the skewness of the vertical velocity w of the filtered fields is negative and lower than the residuals; that is, LCs vorticity and divergence are less skewed than SMCs. We tested a range of filter scales from 300 m to 1 km, and the selection of 550 m comes from visual confirmation of best separation of LCs (and roll-cells) structures from larger scales. We expect this optimal filter scale to depend on horizontal resolution.

LCs and SMCs such as fronts and filaments coexist and interact with one another. During event 1, we report parallel interactions (LCs main axis parallel to a frontal axis) as in Fig. 2c where submesoscale structures do not seem impeded by the LCs development. However, the frontal balance is most likely modified and the LCs are spatially inhomogenous (while the wind and wave forcing are horizontally varying slowly). We further investigate the spatial pattern of LCs in section 4. We also report some orthogonal interactions (with the LCs' main axis orthogonal to a frontal axis) that seem to disrupt fronts (see, e.g., Fig. 3). The destruction processes for fronts or filaments are related to a forward energy cascade and dissipation, and could be induced by frontal arrest, fragmentation by frontal instabilities, vortex formation, and turbulent diffusion. Figure 3 suggests orthogonal LCs lead to frontolysis. During event 2 the surface fields are completely dominated by LCs, and we do not detect any submesoscale front or filament in filtered fields. This is consistent with previous work reporting that strong winds can erode surface density gradients (Sun et al. 2020), but the mechanism for this erosion is still unclear. Wind and SMCs frontal alignment arguments have been invoked by Mahadevan et al. (2010) and Thomas and Lee (2005) and suggest that wind-driven overturning cells could intensify or oppose the secondary circulation of SMCs.

Figure 4 shows the time evolution of the root-mean-square (rms) of the filtered (l_f = 550 m) and residual velocities: the horizontal velocity magnitude $|\mathbf{U}| = \sqrt{u^2 + v^2}$ at surface, with u and v being the horizontal components of the velocity vector in the Cartesian coordinates system (x, y, z) and the vertical velocity w at $z = -10$ m. We choose this depth for w as it is the Stokes drift e-folding average depth (and for consistency with Fig. 12, where w is taken at −10.5 m) to display the same quantities as in Sullivan and McWilliams (2019) and facilitate comparison with their LES results in section 4. The time period shown covers the two large wave events 1 and 2. They are identified by large average wave amplitude $A_{wave} >$ 1.5 m. Event 1 has low winds and event 2 has strong winds with a wind speed $v_{wind} > 10$ m s^{-1}. The rms magnitude of the horizontal velocity of the filtered fields (SMCs and larger-scale flows) does not change much between events (see horizontal blue dashed lines in Fig. 4, second row). But the one associated with the LCs (residuals of the filtering operation) increases significantly between events 1 and 2 (horizontal pink dashed lines in Fig. 4, second row). This reflects that LCs, omnipresent during event 2, have a strong horizontal velocity variance. More importantly, LCs have a very large vertical velocity variance signature exceeding the SMCs (and larger scales) signal as visible on the third row of Fig. 4 with almost none associated with the density gradient field (e.g., Fig. 9a).

c. *Kinetic energy spectrum*

We examine the horizontal $u^2 + v^2$ and vertical w^2 kinetic energy (KE) wavenumber spectra for the five sets of solutions in Fig. 5 during the two large wave events. During event 1 the remote west swell event, the solution with the waves (WEC case; purple lines) captures the large-scale (mesoscale) variability as

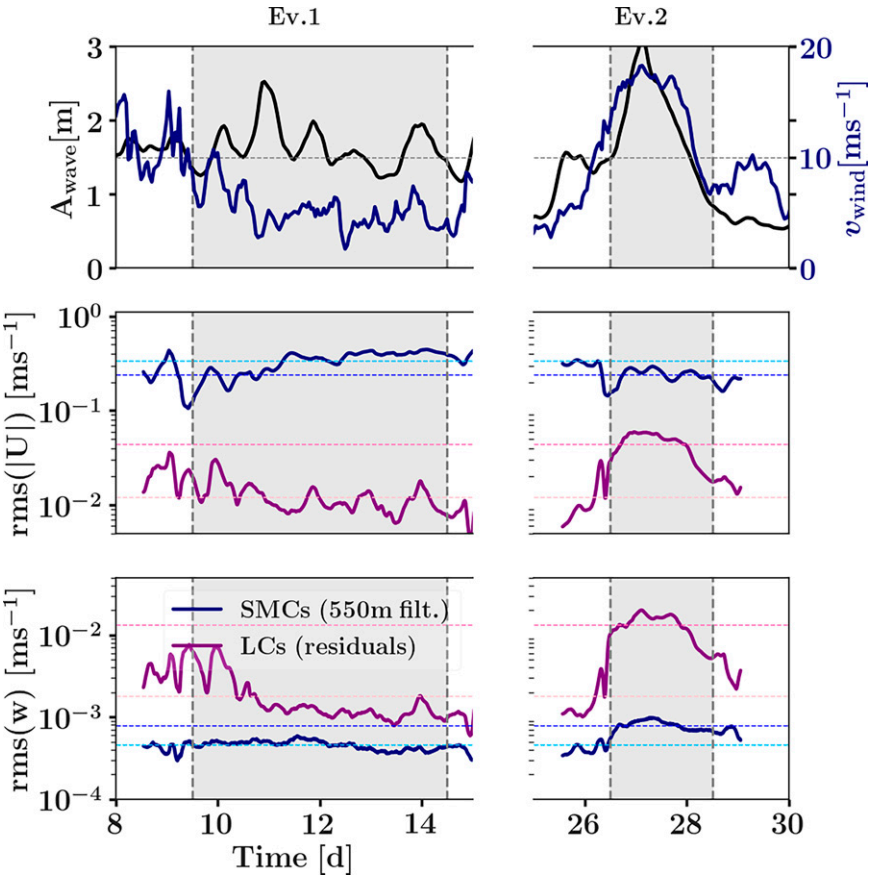

FIG. 4. Time series (days since 0000 LT 1 Dec 2006) of (top) wind speed v_{wind} (blue line; y axis on the right) and wave amplitude A_{wave} (black line; y axis on the left), (middle) root-mean-square of the surface horizontal velocity magnitude, and (bottom) vertical velocity w at $z = -10$ m of the L4 WEC solution. Filtered fields using a 550-m uniform filter are plotted in blue and in purple are the residuals. Solutions are only displayed during high-wave events, i.e., when $A_{wave} > 1.5$ m (gray shaded areas). Light and dark blue dashed lines represent event 1 and 2 time averages, respectively, of the filtered fields. Light and dark pink dashed lines represent event 1 and 2 time averages, respectively, on the residuals.

well as submesoscale (e.g., dashed gray line; $l_f = 550$ m) and smaller-scale variability (e.g., dashed pink line; $l_{LC} = 160$ m), which is the range of scales of the resolved LCs here. The solution without wave forcing (NO WEC case; blue lines), however, underestimates the energy levels at small scales (<1 km) by at least an order of magnitude compared to all the other sets of solutions using KPP. It is precisely because the NO WEC solution does not develop LCs while all the other solutions do with a local maximum of energy level around the average LCs width (dashed pink line). The horizontal KE spectra of the solutions that use the KPP+ scheme (teal lines) shows a substantial energy reduction at small scales, smaller than l_f, compared to the WEC solution during both events, as expected from solutions with increased vertical mixing. The enhanced mixing via KPP+ is associated with a decrease of horizontal velocity gradients, and we observe that root-mean-square surface vorticities are lower when using KPP+ compared to KPP. This effect is due to greater boundary layer mixing rates (diffusivity). Ultimately this yields larger LCs widths (around 200 m) in the KPP+ runs. The local maximum of energy associated with these wider LCs is then shifted toward larger scales in the KPP+ solutions. Energy levels of larger scales are higher with KPP+ than with KPP during event 1, revealing a richer submesoscale and mesoscale activity. This is due here to sampling variability induced by the different boundary conditions used between the WEC KPP and the WEC KPP+ solutions as we use an L3 with KPP+ to force the latter (see Table 1).

For event 1 we compute the KE dissipation rate induced by hyperdiffusion (Lemarié et al. 2012) at the surface in the three hydrostatic solutions NO WEC, WEC, and WEC KPP+ shown in Table 2. The WEC solution has a small-scale KE dissipation rate that is twice as large as in the KPP+ run and 10 times larger than the NO WEC case. This is consistent with the energy levels at small scales for the three solutions with the WEC solution being the most energetic, followed by WEC KPP+ and NO WEC having the lowest energy levels at small scales. This was computed by performing spatial and time averaging. For the KE dissipation by vertical mixing, we compute

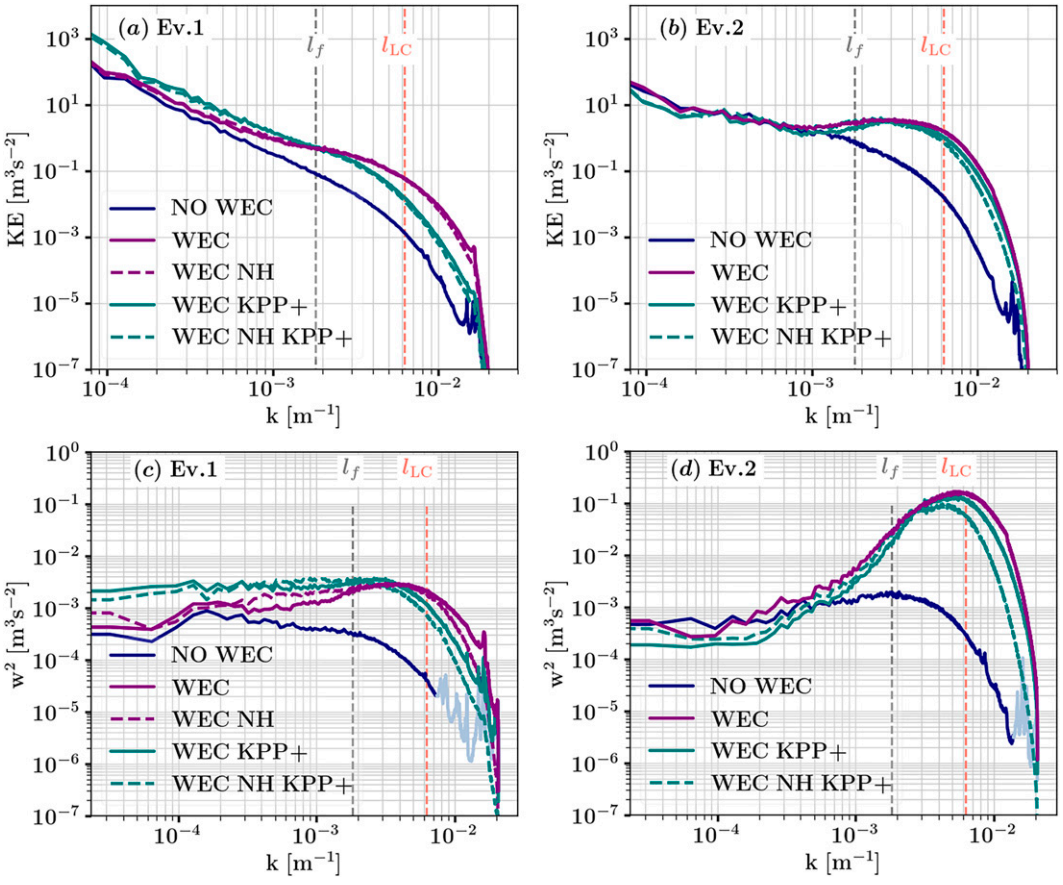

FIG. 5. Time average surface (a),(b) horizontal and (c),(d) vertical (m^2 s^{-2} cpm^{-1}) kinetic energy power spectra during (left) event 1 and (right) event 2. We compare solutions with WEC (purple lines) and without WEC (blue lines). Nonhydrostatic effects are taken into account in the solutions shown with dashed lines and with KPP + in teal. The dashed gray line is positioned at the length scale of the uniform filter $l_f = 550$ m used for Figs. 2 and 4, and the dashed pink line is positioned at the length scale of the width of the LCs as computed in the WEC solutions, i.e., $l_{LC} \simeq 160$ m. The kinetic energy spectra associated with the vertical velocity w are calculated at 10-m depth. We attenuated the color of part of the small scales signal in the NO WEC solution to increase the readability of the other solutions. Note how the nonhydrostatic effects are more evident on vertical velocities at small scales.

the rms value of the spatial averaging. The KPP solutions are found to be more dissipative of horizontal KE by vertical mixing than the KPP+ solution. We observe that LCs are more well defined in KPP runs than in KPP+ runs and, when developed, they are responsible for more KE dissipation. Indeed, the averaged near-surface KE dissipation by vertical mixing as a function of scale peaks at the scales of LCs (not shown).

Event 2, associated with intense winds, favors the wide development of LCs in the entire modeled region for the full duration of the event, up to the point where SMCs are not visible in surface velocity gradient fields at all (in any solution). This is expressed in solutions that include wave effects with surface energy levels showing maxima near l_{LC} (see Figs. 5b,d, purple and teal lines). The spectra of w^2 at −10-m depth (Figs. 5c,d) corroborate our above listed remarks but also reveal nonhydrostatic effects. We find that hydrostatic runs (solid lines) tend to overestimate vertical velocities at small scales compared to nonhydrostatic runs (dashed lines). The overestimation of w by hydrostatic systems has been noted before (e.g., Jeevanjee 2017). But overall, nonhydrostratic effects seem to be minor, and this permits us to focus on hydrostatic runs in the following analysis.

TABLE 2. Time and spatial average of KE dissipation and rms of the spatial average of the vertical mixing of KE (m^2 s^{-3}) at the surface during event 1.

Simulation	NO WEC	WEC	WEC KPP+
KE dissipation	-1.78×10^{-9}	-1.96×10^{-8}	-1.03×10^{-8}
rms KE mixing	1.34×10^{-5}	1.71×10^{-5}	4.12×10^{-6}

During event 1, at $z = -100$ m, spectra from WEC and NO WEC cases tend to be similar revealing that remote swell wave effects on currents are more prominent in the wind-driven mixed layer (Fig. 6a, dotted lines). This is not true during event 2 (Fig. 6b), where there is still large small-scale

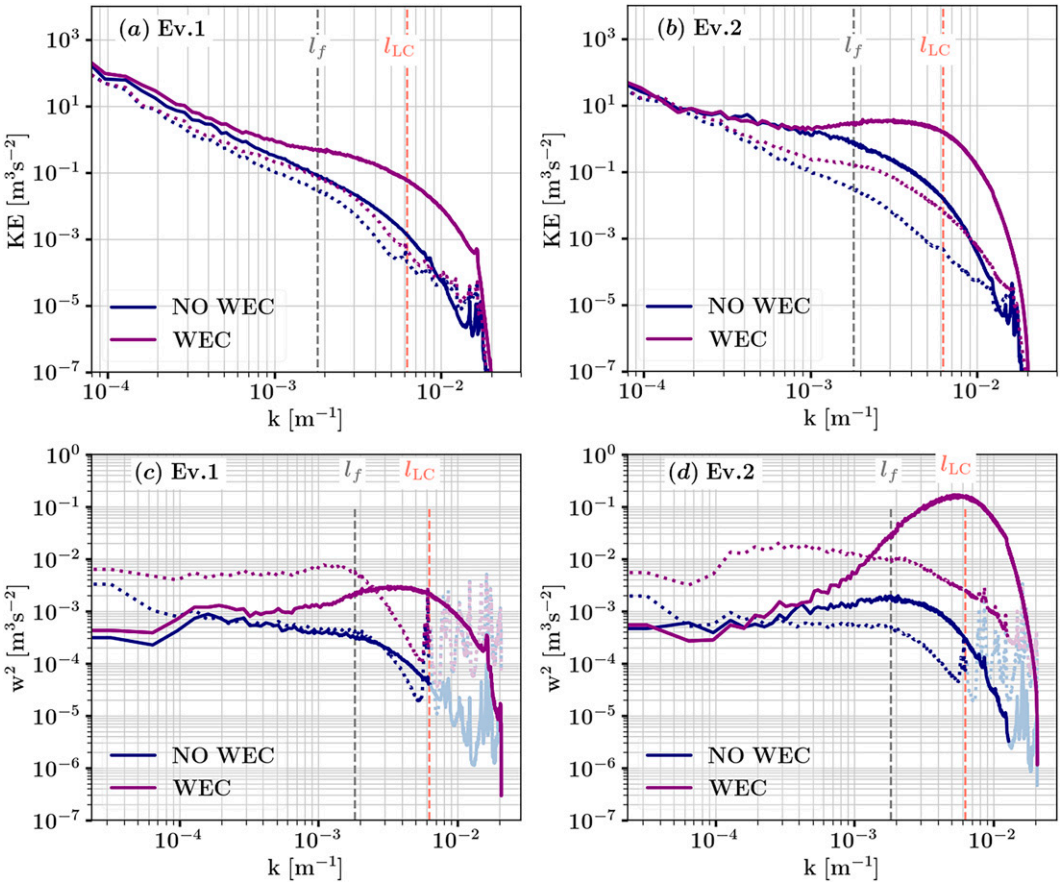

FIG. 6. Time average (a),(b) horizontal and (c),(d) vertical (m^2 s^{-2} cpm^{-1}) kinetic energy power spectra during (a),(c) event 1 and (b),(d) event 2 as in Fig. 5 at the surface (solid lines; at 10-m depth for w) and $z = -100$ m (dotted lines) for the NO WEC and WEC solutions. The dashed gray line is positioned at the length scale of the uniform filter $l_f = 550$ m used for Figs. 2 and 4, and the dashed pink line is positioned at the length scale of the width of the LCs as computed in the WEC solutions, i.e., $l_{LC} \simeq 160$ m. We attenuated the color of part of the small scales signal in the NO WEC solution and the WEC solution at -100 m to increase the readability of the other solutions.

energy in the WEC solution. The vertical velocity spectra at depth (Figs. 6c,d) show a significant increase in mesoscale activity compared to surface levels. This signal may be related to internal gravity waves. The pycnocline internal gravity wave field is enhanced by a factor of 2 or more (>4 during event 2) by WEC. The mechanism behind this could be more active generation of internal waves at the pycnocline by surface layer flows, and LCs in particular.

3. Cross-scale energy transfers

We use a coarse-graining approach (Srinivasan et al. 2022; Aluie et al. 2018; Eyink 2005; Germano 1992) to estimate KE fluxes across scales and particularly across SMCs and LCs scales. Because the 550-m spatial filter can approximately separate SMCs and larger motions from LCs, we choose a spatial-based analysis. We compute the horizontal coarse-grained KE flux across spatial scales as follows:

$$T_h = -\tau_{uv}(\overline{u}_y + \overline{v}_x) - \tau_{uu}\overline{u}_x - \tau_{vv}\overline{v}_y, \tag{2}$$

where $\tau_{uv} = \overline{uv} - \overline{u}\,\overline{v}$ and bars denote uniform spatial filter operations.

In the vertical direction, the KE flux reads

$$T_v = -\tau_{uw}\overline{u}_z - \tau_{vw}\overline{v}_z. \tag{3}$$

With WEC, two extra energy transfer terms appear because of Stokes drift. The horizontal flux associated with Stokes drift is

$$T_h^{\mathrm{St}} = -\tau_{uv}(\overline{u_y^{\mathrm{St}}} + \overline{v_x^{\mathrm{St}}}) - \tau_{uu}\overline{u_x^{\mathrm{St}}} - \tau_{vv}\overline{v_y^{\mathrm{St}}}, \tag{4}$$

and the vertical flux associated with Stokes drift is

$$T_v^{\mathrm{St}} = -\tau_{uw}\overline{u_z^{\mathrm{St}}} - \tau_{vw}\overline{v_z^{\mathrm{St}}}. \tag{5}$$

We show in Fig. 7 coarse-grained KE fluxes as a function of filter scales and depths, averaged horizontally and over event 1. When wave effects are not included (the NO WEC case), the total KE flux $T_h + T_v$ (Fig. 7d, bottom row) changes

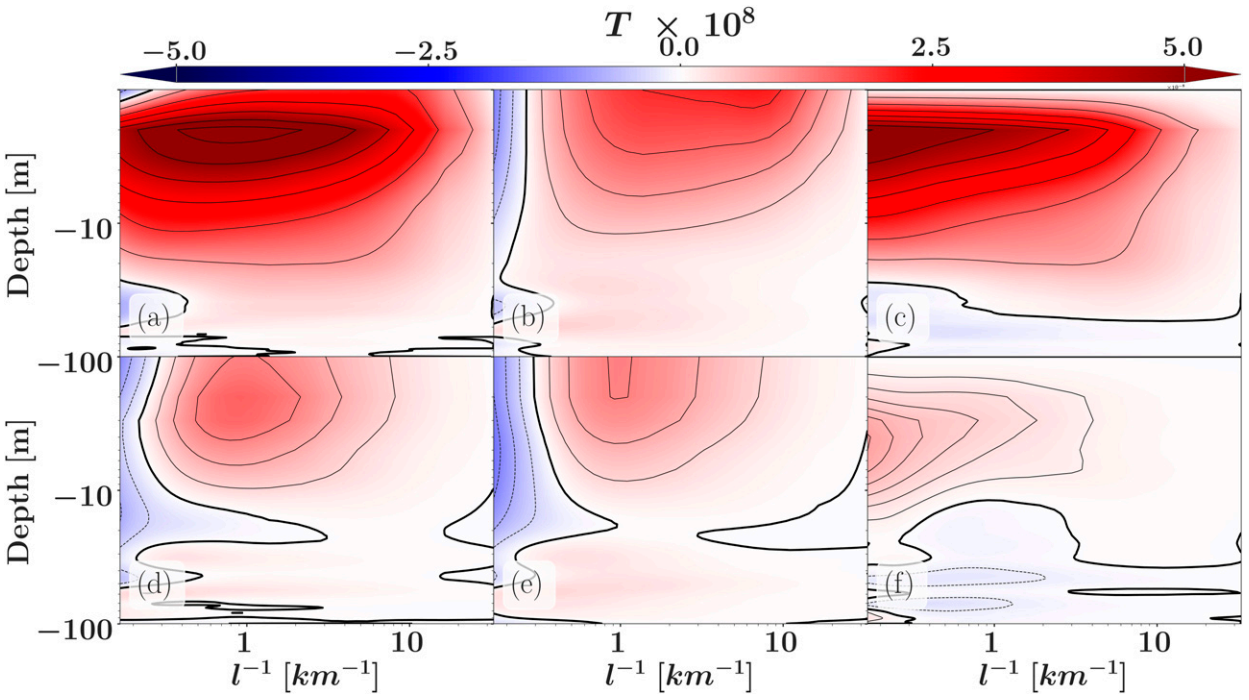

FIG. 7. Depth structure of horizontally and time (event 1) averaged energy fluxes ($m^2\ s^{-3}$) for the (top) WEC and (bottom) NO WEC solutions as a function of the inverse filter scale. (a),(d) The sum of the horizontal and vertical components of the energy transfer terms $T_h + T_v$ from scales finer than a certain scale to coarser scales. Positive (red) value indicates transfer of energy from larger scales to smaller scales, i.e., a forward cascade of energy. Reversely, negative (blue) value indicates inverse cascade of energy. Also shown separately are (b),(e) the horizontal components T_h [Eq. (2)] and (c),(f) the vertical components T_v [Eq. (3)].

sign near the surface and down to 60 m around the 4-km filter scale. For a length scale smaller than 4 km, the energy cascade is forward (from large scales toward small scales) and provides a route to dissipation through frontogenesis (Srinivasan et al. 2022). For scales larger than 4 km, the energy cascade reverses and energy transfers from small scales to the mesoscales and larger. With WEC (Fig. 7d, top row), the vertical energy flux increases drastically near the surface and has a vertical extent of Stokes drift *e*-folding depth (around 10 m here; see Fig. 7c). The horizontal flux is also enhanced (Fig. 7b), which results in a shift of transition between forward and inverse energy cascades to length scales larger than at least 5 km near surface. The inverse cascade is confined to intermediate waters $20 < z < 60$ m for scales larger than 2 km. The enhancement of the horizontal flux T_h with WEC is consistent with results from HRMD21 where WEC was found to increase near-surface horizontal velocity gradients. The horizontal Stokes flux [Eq. (4); not shown] is negligible but the vertical Stokes flux [Eq. (5)] is of leading order and contributes equally to the forward energy cascade at all calculated scales. The computed filter scale upper limit (~6 km) comes from the size of the L4 domain; a bigger domain at this resolution would allow a better determination of the location where the transition to the inverse cascade of energy occurs with WEC. The wave field is a source of energy that goes to small scales in the upper ocean ($z > -20$ m). During event 2, the forward energy cascade occurs down to $z > -100$ m for all the computed filter scales (not shown). This explains why KE levels at mesoscales in solutions with WEC are no larger than the NO WEC levels (e.g., Fig. 5). The inverse energy cascade is not active at these scales; instead energy flows from the wave field to the smaller scales.

The dominant fluxes (T_h, T_v, and T_v^{St}) depth-integrated over the top 100 m are shown in Fig. 8 for both events 1 and 2. A comparison between the WEC and NO WEC solutions (solid/dashed lines) demonstrates that wave forcing enhances the forward cascade (positive fluxes) and reduces the inverse cascade in all cases (the transition toward negative fluxes is pushed toward larger scales) during event 1 (Fig. 8, left panel). The two events differ in the amplitude of the fluxes (by two orders of magnitude) because event 2 is dominated by LCs dynamics. During event 2 (Fig. 8, right panel), fluxes are large and only positive, revealing a direct transfer of energy from large to small scales.

In Fig. 9, we display on the first row snapshots of the density gradient (Fig. 9a), with a clear submesoscale front in the middle, surface normalized vorticity (Fig. 9b), and divergence (Fig. 9c). The latter fields show that LCs are present at that time (during event 1), but they do not imprint on the density gradient field, corroborating that LCs have a relatively weak density (buoyancy) gradient variance associated with them. They also have an inhomogeneous spatial distribution. LCs are more striking, developed on the cold (left side in this figure) side of the front, and less well defined on the right and warm side. We compute the vertically integrated (over the

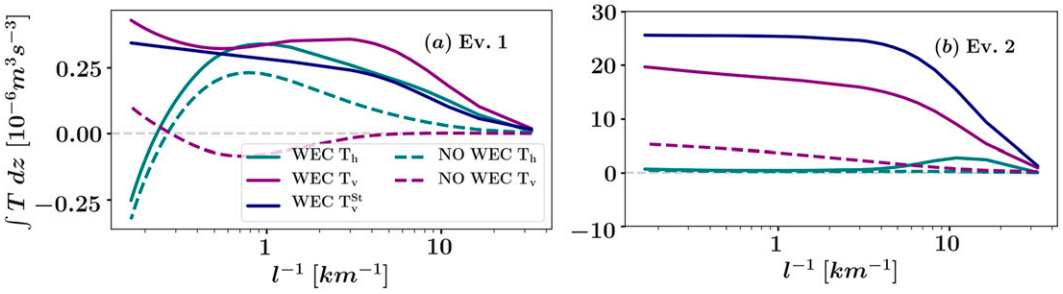

FIG. 8. Depth integrated (over the top 100 m) high wave event averaged coarse-grained kinetic energy (KE) fluxes for (a) event 1 and (b) event 2, where spatial filters are computed using a uniform filter. Depth-integrated fluxes from the NO WEC solutions are the dashed lines, and the ones from the WEC solution are the solid lines. The horizontal transfer term T_h [Eq. (2)] is in teal, the vertical transfer term T_v [Eq. (3)] is in purple, and the vertical transfer term associated with the Stokes drift T_v^{St} [Eq. (5)] is in blue.

first 15 m) dominant fluxes T_h (Fig. 9d), T_v (Fig. 9e), and T_v^{St} (Fig. 9f) at the filter scale $l_f = 550$ m. This reveals that the submesoscale front has a strong signature on the three integrated fluxes: negative on T_v and T_v^{St}, and large positive on T_h. This is in agreement with the work of Srinivasan et al. (2022) that shows that frontogenesis is a mechanism of forward energy cascade at fronts. The new finding here is that LCs imprint solely on the vertical fluxes of energy T_v and T_v^{St} (and not at all on T_h) as evidenced by the clear spatial correlation between where LCs are widely developed in Figs. 9b and 9c and the strong amplitude signal in Figs. 9e and 9f. This indicates that the forward cascade of energy associated with large vertical fluxes in WEC solutions is due to the LCs. This is also evidenced by the vertical structure of the fluxes at the 550-m filter scale in Fig. 10. The vertical fluxes peak near surface as a result of the wave forcing on a vertical scale on the order of the Stokes drift *e*-folding depth (around 10 m here). Meanwhile, the horizontal flux has a larger vertical extent (down to the entire mixed layer; 50–80 m here) as dictated by SMCs vertical extent (more evident during event 1 because event 2 is depleted in SMC structures).

Solutions using KPP+ develop larger LCs ($l_{\mathrm{LC}} = 200$ m) with similar inhomogeneous patterns compared to solutions with KPP ($l_{\mathrm{LC}} = 160$ m). We find that the LCs extend deeper vertically, which is allowed by the deeper surface mixed-layer depth (evidenced by the tail of the log PDF of the surface mixed-layer depth of the different solutions; not shown) rather than in the solutions with KPP. This explains why the kinetic energy transfer terms T_h, T_v, and T_v^{St} are very large and positive near surface and at depth for KPP+ solutions during event 1 (not shown because it is similar to Fig. 8, but with terms that are mainly positive and have slightly larger amplitudes). It leads to $T_h + T_v > 0$ (i.e., a forward energy cascade) from the surface down to 100-m depth and for all the

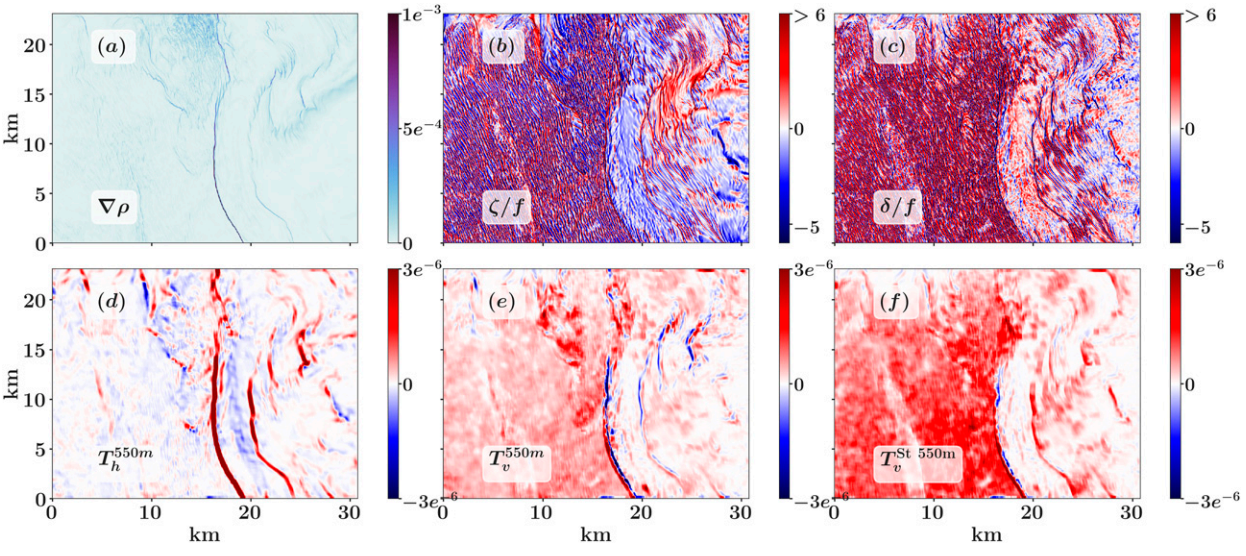

FIG. 9. Snapshots of the surface (a) density gradient (kg m^{-4}), (b) normalized vorticity, and (c) normalized divergence at 0620 LT 11 Dec 2006 (event 1). Structures of the (d) horizontal T_h [Eq. (2)], (e) vertical T_v [Eq. (3)], and (f) Stokes vertical T_v^{St} [Eq. (5)] cross scales energy transfer terms vertically integrated over the first 15 m (m^3 s^{-3}) at the $l_f = 550$ m filter scale.

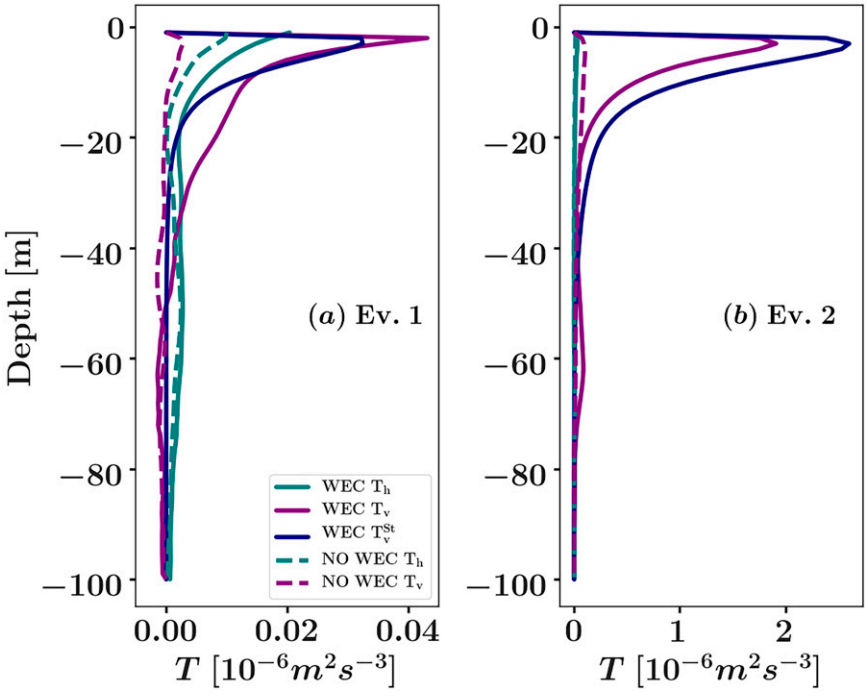

FIG. 10. Depth structures of the horizontal T_h [Eq. (2); teal lines], vertical T_v [Eq. (3); purple lines], and Stokes vertical T_v^{St} [Eq. (5); blue lines] cross-scale energy transfer terms ($m^2\ s^{-3}$) during (a) event 1 and (b) event 2 from the NO WEC (dashed lines) and WEC (solid lines) solutions at the $l_f = 550$ m filter scale.

filter scales computed here (as shown in Fig. 8). LC development, favored in deep surface mixed layer, generates this forward energy cascade.

Nonhydrostatic solutions have, on average, sparser and weaker LCs associated with slightly lower-amplitude vertical velocities compared to hydrostatic solutions. This occurs simultaneously with a more powerful SMCs field (see, e.g., Fig. 2c), which could be due to fewer frontolytic interactions of LCs and SMCs. Ultimately, this induces a less powerful forward energy cascade associated with LCs rather than in hydrostatic solutions. As an example at the time shown in Fig. 7, the vertically integrated energy fluxes have a similar spatial distribution but with smaller amplitudes. Computed as a relative difference between the hydrostatic solution and nonhydrostatic solution, we find a decrease of 7% in the vertical flux of energy T_v when averaging horizontally and an 11% decrease for the vertical flux associated with the Stokes drift T_v^{St}. When computing the summation of $T_h + T_v + T_v^{St}$ at the 550-m filter scale, we find a decrease of 13% in the nonhydrostatic forward cascade of energy compared to the hydrostatic one on average.

4. Langmuir pattern

In Figs. 9b and 9c, the flow shows subareas with distinct velocity patterns: on the cold side of the submesoscale front, positioned approximately in the middle of the snapshot in Fig. 9a, LCs are well developed while they are weaker on the warm side. The SMC structure seems to act as a barrier for LCs. We show in section 3 that the cold side is associated with large vertical fluxes of KE energy. In particular, the terms τ_{uw} and τ_{vw} in Eqs. (3) and (5) are large (and dominant compared to the vertical shear terms) on that side due to the large vertical velocity w associated with the LCs. We also report that the cold (warm) side is associated with lower (larger) vertical shear, larger (lower) vertical mixing, and deeper (shallower) mixed layer depth. This leads to the inference that with large wave and or wind forcings where KPP enables more vertical mixing with deeper mixed layer the LCs seem to develop more strikingly, with large w and thus large positive vertical energy fluxes. This ultimately provokes a forward cascade of energy that we discuss in section 3 and a route to dissipation.

The front, shown in Fig. 9, is aligned with the propagating west swell waves at the time of event 1. We zoom into a region centered along the front and perform an alongfront averaging in Figs. 11a–c and 12, left panel first row. Below, we show the downwelling velocity $w < 0$ at $z = -10.5$ m in that region. The frontal density gradient is positive along the x axis, and the mixed layer depth deepens from -20 m on the warm side to -40 m in average on the cold dense side (while at the front the convergence reaches down to -55 m). In this case of alongfront propagating waves ($v^{St} > 0$, $u^{St} \sim 0$), we observe that the major axes of the cells are parallel to the frontal axis (labeled parallel case). On the warm side of the frontal axis, where the cells are less striking, the width l_{LC} between downwelling lines shrinks as x increases. These changes

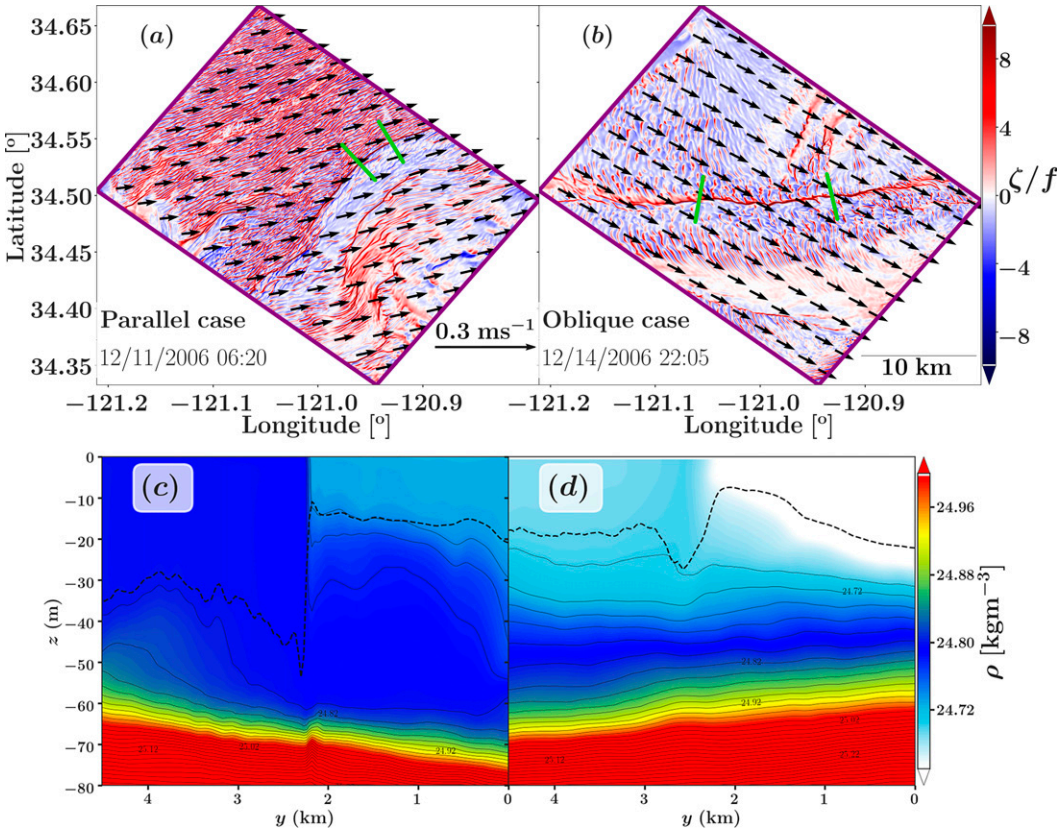

FIG. 11. Snapshots of normalized vorticity on the (a) 0620 LT 11 Dec 2006 (as in Fig. 9) and (b) 2205 LT 14 Dec 2006 (as in Fig. 3c) events (both event 1). Surface Stokes drift is superimposed as arrows. The green lines demarcate the portion of the flow we use when alongfront averaging in (c) and (d) and in Fig. 12. (c),(d) Cross sections of alongfront averaged density for the selected portion of the fronts in (a) and (b), respectively. We show alongfront averaged isopycnals in black solid lines and mixed layer depth in black bold dashed lines. Note that the x axis increases leftward. In both (c) and (d), the LCs develop more strikingly on the cold and dense side of the fronts where the mixed layer is on average deeper.

of the LC patterns appear to correlate with a sharp change of the secondary circulation $\langle u \rangle$ (crossfront velocity; black lines) decreasing as x increases and in the alongfront (positive) jet $\langle v \rangle$ (alongfront velocity; cyan lines). In previous work, Sullivan and McWilliams (2019) found correlation with the growth of the secondary circulation $\langle u \rangle$ and the down-filament (negative) jet $\langle v \rangle$ but in a misaligned waves and surface currents case. They speculated that the wave–current misalignment inhibited LCs development similar to Sullivan et al. (2012) and Van Roekel et al. (2012).

We examine a misaligned case (labeled oblique case) in Figs. 11b–d and in the right panel of Fig. 12 where both v^{St} and $u^{St} \neq 0$. It is the front shown in Fig. 3c, where LCs develop orthogonally close to the frontal axis. Similarly, as in the previous case, the dense and cold side of the front is displayed on the left, and the LCs have developed more strikingly than on the right and warm side of the front. In this case, the secondary circulation is close to an idealized case, with $\langle u \rangle$ changing sign near the front location, whereas in the aligned case a strong background velocity makes $\langle u \rangle$ only positive. Here the alongfront jet is downfront (negative) and more powerful on the cold side with strong LCs, which is the opposite as in the aligned case. It is therefore difficult based on these two examples to assess which far-field horizontal velocities make favorable LCs development conditions. Instead, the development (or inhibition) of LCs seems to be primarily correlated with large (weak) vertical mixing, deep (shallow) mixed layer depth and large (weak) vertical velocities.

5. Conclusions

We perform submesoscale-resolving oceanic simulations with ROMS in a region offshore of Pt. Conception in central California with $\Delta x = 30$ m horizontal grid resolution. We take into account surface gravity wave effects on currents using the vortex force formalism and an efficient approximation of the Stokes drift based on 2D directional wave spectra derived with WW3. This analysis is based on five model solutions and assesses the relative importance of the wave effects on currents, nonhydrostatic effects, and the changes induced by a partially Langmuir turbulence enhanced version of the K-profile parameterization (KPP vs KPP+) vertical mixing scheme.

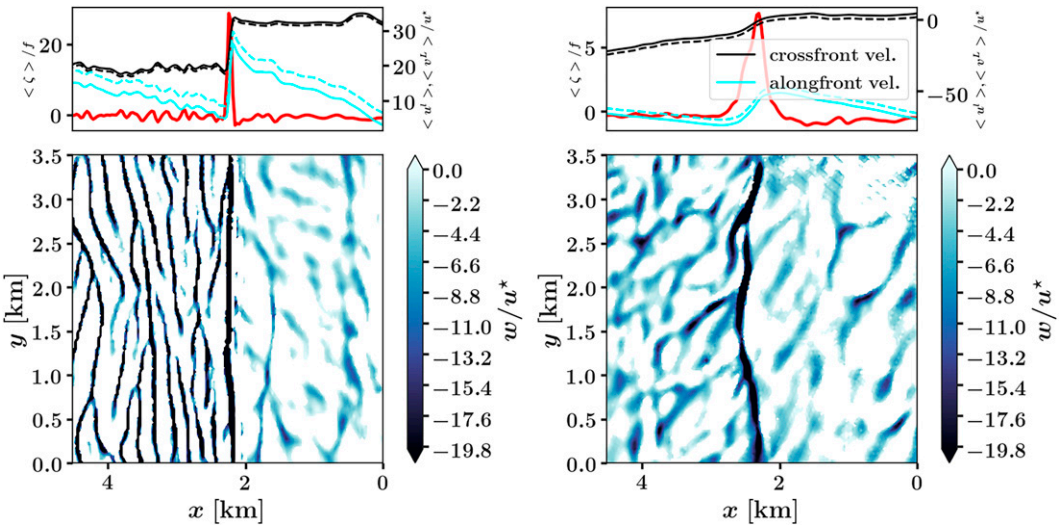

FIG. 12. The first row shows the crossfront variation of the average vertical vorticity $\langle\zeta\rangle/f$ (red lines; axis on the left), the average crossfront Lagrangian current $\langle u^L\rangle/u^\star$ (dashed black lines; axis on the right), and the average alongfront Lagrangian current $\langle v^L\rangle/u^\star$ (dashed cyan lines; axis on the right) when normalized by the friction velocity $u^\star$ Solid black and cyan lines are the corresponding Eulerian average currents, so the difference between solid and dashed lines is the Stokes drift components. The vorticity is at surface, and currents are at $z \sim -5$ m. The second row shows the instantaneous downwelling velocity $w/u^\star < 0$ at $z = -10.5$ m. We match notations as in Fig. 9 of Sullivan and McWilliams (2019) to facilitate comparison. Note that the x axis increases leftward. Shown are (left) the parallel (main axis of LCs parallel to the frontal axis) case at 0620 LT 11 Dec 2006 (event 1) as in Figs. 11a and 9 and (right) an oblique (main axis of LCs not parallel to the frontal axis) case at 2205 LT 14 Dec 2006 (event 1) as in Figs. 11b and 3c.

We find that when waves (or winds) are large, solutions manifest Langmuir cells (LCs). These cells take the form of oblong convergence zones with large vertical velocities and a spacing between lines of $l_{\rm LC} = 160$ m in the hydrostatic solution with waves using KPP. In solutions using the KPP+ scheme, the LCs are somewhat wider, $l_{\rm LC} = 200$ m. They develop inhomogeneously depending on the wave and wind forcing amplitudes as well as the currents present. Once developed they are advected by the mean flow. We report interactions between LCs and submesoscale structures: when the main axis of the LCs is parallel to a front or filament axis they coexist, while when the main axis of the LCs is orthogonal to a front or filament axis they can be disrupted by LCs. We analyze here two large wave events: one associated with a remotely generated swell (event 1) and one associated with local wind-generated waves (event 2). The latter is characterized by LCs in the entire region together with a scarcity of submesoscale features. A spatial filter at 550 m separates the LC signal from the SMCs and larger-scale flow. The residual of this filtering process (containing the LCs) results in very large horizontal and vertical velocity variances not associated with the density gradient field. Solutions that include wave effects on currents show a peak of kinetic energy at the length scale $l_{\rm LC}$ during both events. The KPP+ scheme is responsible for a shift of this peak toward larger scales due to its enhanced vertical mixing rate. At depth, the LC signal vanishes as they are confined to the mixed layer, as are the SMCs. We show that the development of LCs enhances a forward cascade of kinetic energy using a coarse-graining technique based on spatial filtering. This forward cascade is predominantly active in the upper ocean for horizontal scales up to 5 km. This vertical extent corresponds to both the Stokes drift e-folding and the Ekman depth here. In the solution not including waves, the forward energy cascade transitions to an inverse cascade of energy around a slightly smaller length of 4 km, and the forward cascade rate is much weaker. We find that the LCs are responsible for this change and the forward energy cascade, due to the large vertical velocities associated with them and the energy conversion associated with SMCs and larger-scale vertical shear. It translates into large and dominating vertical fluxes spatially correlated with areas where LCs develop widely. Submesoscale features imprint through the entire mixed layer on the vertical and horizontal energy fluxes, providing a route to dissipation through frontogenesis. The distribution of the LCs seems to be correlated with a deep mixed layer, in the sense that LCs are more numerous and striking in a deeper mixed layer, associated with large vertical velocities.

Nonhydrostatic effects are noticeable on small-scale vertical velocities. Here we find that hydrostatic solutions tend to overestimate w at small scales near surface. For this reason nonhydrostatic configurations have less powerful LCs and associated forward energy cascade than do hydrostatic ones. No doubt nonhydrostatic dynamics would become stronger with even finer grid resolution, but it is remarkable how minor its influence is in the present simulations.

This analysis provides a comparison for two vertical mixing schemes, KPP versus KPP+, in realistic oceanic settings; the latter is better justified in the presence of waves (Li et al.

2019). Here we report that KPP+ and KPP solutions are very similar, yet KPP+ leads to slightly wider LCs, associated with smaller surface velocity gradients. This indicates that further attention is warranted to mixing parameterizations in Langmuir turbulence.

The present simulations have a grid resolution that would be considered coarse for LCs, since we only partially resolve the w field, but fine for SMCs compared to current practices. There is a fundamental dilemma in modeling the transition from circulation to boundary layer turbulence, that is, how to modify the subgrid-scale parameterization as Δx decreases (Wyngaard 2004). In this study we have not made such a modification and thus are likely double counting some of the LC effects by both partly resolving and parameterizing them with KPP+. Yet, the computational cost of using very fine resolution for a realistically interacting field of SMCs is presently prohibitive. This is a topic for future research.

A limitation of the present analysis is the fact that it is based on only two large wave events and therefore lacks a broad view of possible outcomes. Idealized studies with both LCs and a submesoscale front or filament with a KPP+ boundary layer parameterization could further clarify the influences on LC inhomogeneity. Another limitation is the artificial decoupling of the wind, wave, and current evolutions, thereby excluding the current effects on waves (CEW) (e.g., Romero et al. 2020, 2017; Vrećica et al. 2022) or effects on winds (e.g., Renault et al. 2016). This is another topic for future research.

Acknowledgments. We thank Kaushik Srinivasan for the helpful discussions on the coarse graining approach and Peng Wang, who created the KPP+, implemented it in ROMS, and is writing a paper on this KPP+. We also would like to thank Eric D'Asaro and Andrey Shcherbina for making available to us observational data. Anonymous reviewers helped improving this manuscript and we thank them too. This work used the Extreme Science and Engineering Discovery Environment (XSEDE; Towns et al. 2014), which is supported by National Science Foundation Grant ACI-1548562, Expanse through the allocation Oceanic Circulation Across Multiple Scales TG-OCE030000N. This research is supported by the National Science Foundation (NSF Grants OCE-1355970 and OCE-2124174) and the U.S. Office of Naval Research (ONR Grants N00014-14-1-0626 and N00014-15-1-2645). Leonel Romero was supported by grants from the NSF (OCE-1924686 and OCE-2121646).

Data availability statement. The numerical model simulations upon which this study is based are too large to archive or to transfer. Instead, we provide all the information needed to replicate the simulations; we used UCLA ROMS. The model code, compilation script, initial and boundary condition files, and the namelist settings are available upon request.

REFERENCES

Aluie, H., M. Hecht, and G. K. Vallis, 2018: Mapping the energy cascade in the North Atlantic Ocean: The coarse-graining approach. *J. Phys. Oceanogr.*, **48**, 225–244, https://doi.org/10.1175/JPO-D-17-0100.1.

Belcher, S. E., and Coauthors, 2012: A global perspective on Langmuir turbulence in the ocean surface boundary layer. *Geophys. Res. Lett.*, **39**, L18605, https://doi.org/10.1029/2012GL052932.

Capet, X., J. C. McWilliams, M. J. Molemaker, and A. F. Shchepetkin, 2008: Mesoscale to submesoscale transition in the California current system. Part I: Flow structure, eddy flux, and observational tests. *J. Phys. Oceanogr.*, **38**, 29–43, https://doi.org/10.1175/2007JPO3671.1.

Craik, A. D. D., 1977: The generation of Langmuir circulations by an instability mechanism. *J. Fluid Mech.*, **81**, 209–223, https://doi.org/10.1017/S0022112077001980.

——, and S. Leibovich, 1976: A rational model for Langmuir circulations. *J. Fluid Mech.*, **73**, 401–426, https://doi.org/10.1017/S0022112076001420.

Dauhajre, D. P., J. C. McWilliams, and Y. Uchiyama, 2017: Submesoscale coherent structures on the continental shelf. *J. Phys. Oceanogr.*, **47**, 2949–2976, https://doi.org/10.1175/JPO-D-16-0270.1.

Egbert, G. D., and S. Y. Erofeeva, 2002: Efficient inverse modeling of barotropic ocean tides. *J. Atmos. Oceanic Technol.*, **19**, 183–204, https://doi.org/10.1175/1520-0426(2002)019<0183:EIMOBO>2.0.CO;2.

——, A. F. Bennett, and M. G. Foreman, 1994: TOPEX/POSEIDON tides estimated using a global inverse model. *J. Geophys. Res.*, **99**, 24 821–24 852, https://doi.org/10.1029/94JC01894.

Eyink, G. L., 2005: Locality of turbulent cascades. *Physica D*, **207**, 91–116, https://doi.org/10.1016/j.physd.2005.05.018.

Germano, M., 1992: Turbulence: The filtering approach. *J. Fluid Mech.*, **238**, 325–336, https://doi.org/10.1017/S0022112092001733.

Grant, A. L., and S. E. Belcher, 2009: Characteristics of Langmuir turbulence in the ocean mixed layer. *J. Phys. Oceanogr.*, **39**, 1871–1887, https://doi.org/10.1175/2009JPO4119.1.

Gula, J., M. J. Molemaker, and J. C. McWilliams, 2014: Submesoscale cold filaments in the Gulf Stream. *J. Phys. Oceanogr.*, **44**, 2617–2643, https://doi.org/10.1175/JPO-D-14-0029.1.

Hamlington, P. E., L. P. Van Roekel, B. Fox-Kemper, K. Julien, and G. P. Chini, 2014: Langmuir–submesoscale interactions: Descriptive analysis of multiscale frontal spindown simulations. *J. Phys. Oceanogr.*, **44**, 2249–2272, https://doi.org/10.1175/JPO-D-13-0139.1.

Haney, S., B. Fox-Kemper, K. Julien, and A. Webb, 2015: Symmetric and geostrophic instabilities in the wave-forced ocean mixed layer. *J. Phys. Oceanogr.*, **45**, 3033–3056, https://doi.org/10.1175/JPO-D-15-0044.1.

Harcourt, R. R., and E. A. D'Asaro, 2008: Large-eddy simulation of Langmuir turbulence in pure wind seas. *J. Phys. Oceanogr.*, **38**, 1542–1562, https://doi.org/10.1175/2007JPO3842.1.

Hypolite, D., L. Romero, J. C. McWilliams, and D. P. Dauhajre, 2021: Surface gravity wave effects on submesoscale currents in the open ocean. *J. Phys. Oceanogr.*, **51**, 3365–3383, https://doi.org/10.1175/JPO-D-20-0306.1.

Jeevanjee, N., 2017: Vertical velocity in the gray zone. *J. Adv. Model. Earth Syst.*, **9**, 2304–2316, https://doi.org/10.1002/2017MS001059.

Klein, P., and G. Lapeyre, 2009: The oceanic vertical pump induced by mesoscale and submesoscale turbulence. *Annu. Rev. Mar. Sci.*, **1**, 351–375, https://doi.org/10.1146/annurev.marine.010908.163704.

Langmuir, I., 1938: Surface motion of water induced by wind. *Science*, **87**, 119–123, https://doi.org/10.1126/science.87.2250.119.

Large, W. G., J. C. McWilliams, and S. C. Doney, 1994: Oceanic vertical mixing: A review and a model with a nonlocal boundary layer parameterization. *Rev. Geophys.*, **32**, 363–403, https://doi.org/10.1029/94RG01872.

Lemarié, F., J. Kurian, A. F. Shchepetkin, M. J. Molemaker, F. Colas, and J. C. McWilliams, 2012: Are there inescapable issues prohibiting the use of terrain-following coordinates in climate models? *Ocean Modell.*, **42**, 57–79, https://doi.org/10.1016/j.ocemod.2011.11.007.

Li, K., Z. Zhang, G. Chini, and G. Flierl, 2012: Langmuir circulation: An agent for vertical restratification? *J. Phys. Oceanogr.*, **42**, 1945–1958, https://doi.org/10.1175/JPO-D-11-0225.1.

Li, Q., and B. Fox-Kemper, 2017: Assessing the effects of Langmuir turbulence on the entrainment buoyancy flux in the ocean surface boundary layer. *J. Phys. Oceanogr.*, **47**, 2863–2886, https://doi.org/10.1175/JPO-D-17-0085.1.

——, and Coauthors, 2019: Comparing ocean surface boundary vertical mixing schemes with Langmuir turbulence. *J. Adv. Model. Earth Syst.*, **11**, 3545–3592, https://doi.org/10.1029/2019MS001810.

Mahadevan, A., A. Tandon, and R. Ferrari, 2010: Rapid changes in mixed layer stratification driven by submesoscale instabilities and winds. *J. Geophys. Res.*, **115**, C03017, https://doi.org/10.1029/2008JC005203.

McWilliams, J. C., 2016: Submesoscale currents in the ocean. *Proc. Roy. Soc.*, **472A**, 20160117, https://doi.org/10.1098/rspa.2016.0117.

——, 2018: Surface wave effects on submesoscale fronts and filaments. *J. Fluid Mech.*, **843**, 479–517, https://doi.org/10.1017/jfm.2018.158.

——, and B. Fox-Kemper, 2013: Oceanic wave-balanced surface fronts and filaments. *J. Fluid Mech.*, **730**, 464–490, https://doi.org/10.1017/jfm.2013.348.

——, P. P. Sullivan, and C.-H. Moeng, 1997: Langmuir turbulence in the ocean. *J. Fluid Mech.*, **334**, 1–30, https://doi.org/10.1017/S0022112096004375.

——, J. M. Restrepo, and E. M. Lane, 2004: An asymptotic theory for the interaction of waves and currents in coastal waters. *J. Fluid Mech.*, **511**, 135–178, https://doi.org/10.1017/S0022112004009358.

——, E. Huckle, J. Liang, and P. P. Sullivan, 2014: Langmuir turbulence in swell. *J. Phys. Oceanogr.*, **44**, 870–890, https://doi.org/10.1175/JPO-D-13-0122.1.

Ménesguen, C., S. Le Gentil, P. Marchesiello, and N. Ducousso, 2018: Destabilization of an oceanic meddy-like vortex: Energy transfers and significance of numerical settings. *J. Phys. Oceanogr.*, **48**, 1151–1168, https://doi.org/10.1175/jpo-d-17-0126.1.

Michalakes, J., J. Dudhia, D. Gill, J. Klemp, and W. Skamarock, 1998: Design of a next-generation regional weather research and forecast model. *Towards Teracomputing*, N. Kreitz and W. Zwieflhofer, Eds., World Scientific, 117–124.

Renault, L., M. J. Molemaker, J. C. McWilliams, A. F. Shchepetkin, F. Lemarié, D. Chelton, S. Illig, and A. Hall, 2016: Modulation of wind work by oceanic current interaction with the atmosphere. *J. Phys. Oceanogr.*, **46**, 1685–1704, https://doi.org/10.1175/JPO-D-15-0232.1.

Romero, L., Y. Uchiyama, J. C. Ohlmann, J. C. McWilliams, and D. A. Siegel, 2013: Simulations of nearshore particle-pair dispersion in Southern California. *J. Phys. Oceanogr.*, **43**, 1862–1879, https://doi.org/10.1175/JPO-D-13-011.1.

——, L. Lenain, and W. K. Melville, 2017: Observations of surface wave–current interaction. *J. Phys. Oceanogr.*, **47**, 615–632, https://doi.org/10.1175/JPO-D-16-0108.1.

——, D. Hypolite, and J. C. McWilliams, 2020: Submesoscale current effects on surface waves. *Ocean Modell.*, **153**, 101662, https://doi.org/10.1016/j.ocemod.2020.101662.

——, ——, and ——, 2021: Representing wave effects on currents. *Ocean Modell.*, **167**, 101873, https://doi.org/10.1016/j.ocemod.2021.101873.

Roullet, G., J. M. Molemaker, N. Ducousso, and T. Dubos, 2017: Compact symmetric Poisson equation discretization for nonhydrostatic sigma coordinates ocean model. *Ocean Modell.*, **118**, 107–117, https://doi.org/10.1016/j.ocemod.2017.09.001.

Schubert, R., J. Gula, R. J. Greatbatch, B. Baschek, and A. Biastoch, 2020: The submesoscale kinetic energy cascade: Mesoscale absorption of submesoscale mixed layer eddies and frontal downscale fluxes. *J. Phys. Oceanogr.*, **50**, 2573–2589, https://doi.org/10.1175/JPO-D-19-0311.1.

Shchepetkin, A. F., and J. C. McWilliams, 2005: The Regional Oceanic Modeling System (ROMS): A split-explicit, free-surface, topography-following-coordinate oceanic model. *Ocean Modell.*, **9**, 347–404, https://doi.org/10.1016/j.ocemod.2004.08.002.

Shrestha, K., W. Anderson, A. Tejada-Martinez, and J. Kuehl, 2019: Orientation of coastal-zone Langmuir cells forced by wind, wave and mean current at variable obliquity. *J. Fluid Mech.*, **879**, 716–743, https://doi.org/10.1017/jfm.2019.683.

Skyllingstad, E. D., and R. Samelson, 2012: Baroclinic frontal instabilities and turbulent mixing in the surface boundary layer. Part I: Unforced simulations. *J. Phys. Oceanogr.*, **42**, 1701–1716, https://doi.org/10.1175/JPO-D-10-05016.1.

Smith, K. M., P. E. Hamlington, and B. Fox-Kemper, 2016: Effects of submesoscale turbulence on ocean tracers. *J. Geophys. Res. Oceans*, **121**, 908–933, https://doi.org/10.1002/2015JC011089.

Srinivasan, K., R. Barkan, and J. C. McWilliams, 2022: A forward energy flux at submesoscales driven by frontogenesis. *J. Phys. Oceanogr.*, https://doi.org/10.1175/JPO-D-22-0001.1, in press.

Sullivan, P. P., and J. C. McWilliams, 2010: Dynamics of winds and currents coupled to surface waves. *Annu. Rev. Fluid Mech.*, **42**, 19–42, https://doi.org/10.1146/annurev-fluid-121108-145541.

——, and ——, 2019: Langmuir turbulence and filament frontogenesis in the oceanic surface boundary layer. *J. Fluid Mech.*, **879**, 512–553, https://doi.org/10.1017/jfm.2019.655.

——, L. Romero, J. C. McWilliams, and W. K. Melville, 2012: Transient evolution of Langmuir turbulence in ocean boundary layers driven by hurricane winds and waves. *J. Phys. Oceanogr.*, **42**, 1959–1980, https://doi.org/10.1175/JPO-D-12-025.1.

Sun, D., and Coauthors, 2020: Diurnal cycling of submesoscale dynamics: Lagrangian implications in drifter observations and model simulations of the northern Gulf of Mexico. *J. Phys. Oceanogr.*, **50**, 1605–1623, https://doi.org/10.1175/JPO-D-19-0241.1.

Suzuki, N., and B. Fox-Kemper, 2016: Understanding Stokes forces in the wave-averaged equations. *J. Geophys. Res. Oceans*, **121**, 3579–3596, https://doi.org/10.1002/2015JC011566.

——, ——, P. E. Hamlington, and L. P. Van Roekel, 2016: Surface waves affect frontogenesis. *J. Geophys. Res. Oceans*, **121**, 3597–3624, https://doi.org/10.1002/2015JC011563.

Thomas, L. N., and C. M. Lee, 2005: Intensification of ocean fronts by down-front winds. *J. Phys. Oceanogr.*, **35**, 1086–1102, https://doi.org/10.1175/JPO2737.1.

——, A. Tandon, and A. Mahadevan, 2008: Submesoscale processes and dynamics. *Ocean Modeling in an Eddying Regime, Geophys. Monogr.*, Vol. 177, Amer. Geophys. Union, 17–38.

Thorpe, S. A., 2004: Langmuir circulation. *Annu. Rev. Fluid Mech.*, **36**, 55–79, https://doi.org/10.1146/annurev.fluid.36.052203.071431.

Towns, J., and Coauthors, 2014: XSEDE: Accelerating scientific discovery. *Comput. Sci. Eng.*, **16**, 62–74, https://doi.org/10.1109/MCSE.2014.80.

Uchiyama, Y., J. C. McWilliams, and A. F. Shchepetkin, 2010: Wave–current interaction in an oceanic circulation model with a vortex-force formalism: Application to the surf zone. *Ocean Modell.*, **34**, 16–35, https://doi.org/10.1016/j.ocemod.2010.04.002.

Van Roekel, L. P., B. Fox-Kemper, P. P. Sullivan, P. E. Hamlington, and S. R. Haney, 2012: The form and orientation of Langmuir cells for misaligned winds and waves. *J. Geophys. Res.*, **117**, C05001, https://doi.org/10.1029/2011JC007516.

Vrećica, T., N. Pizzo, and L. Lenain, 2022: Observations of strongly modulated surface wave and wave breaking statistics at a submesoscale front. *J. Phys. Oceanogr.*, **52**, 289–304, https://doi.org/10.1175/JPO-D-21-0125.1.

Wu, X., F. Feddersen, and S. N. Giddings, 2021: Characteristics and dynamics of density fronts over the inner to midshelf under weak wind conditions. *J. Phys. Oceanogr.*, **51**, 789–808, https://doi.org/10.1175/JPO-D-20-0162.1.

Wyngaard, J. C., 2004: Toward numerical modeling in the "terra incognita". *J. Atmos. Sci.*, **61**, 1816–1826, https://doi.org/10.1175/1520-0469(2004)061<1816:TNMITT>2.0.CO;2.